Supplementary Information

Constructing TiO_2 nanotube arrays with oxygen vacancies on Cu mesh to enable homogeneous Li deposition towards long-life Li metal anode

Yujue Wang[a], Xiaoping Xian[b], Yilin Wang[b], Yong Guo[c], Dan Xiao[a,c,*]

[a] *Institute of Advanced Study, Chengdu University, Chengdu 610106, China*

[b] *School of Mechanical Engineering, Chengdu University, Chengdu 610106, China*

[c] *College of Chemistry, Sichuan University, Chengdu 610065, China*

* Corresponding authors at: Institute of Advanced Study, Chengdu University, Chengdu 610106, China and College of Chemistry, Sichuan University, Chengdu 610065, China (D. Xiao).

E-mail addresses: xiaodan@scu.edu.cn (D. Xiao).

Detailed descriptions for DFT binding energy analysis:

The difference in lithiophilicity of TNT or Cu was studied by using the binding energy analysis method based on density functional theory (DFT). In the DMol3 module of Materials Studio software, we use general gradient approximation (GGA) [3, 4] and the Perdew-Burke-Ernzerhof (PBE) exchange-correlation functional for first principles calculations. Double numeric with the polarization (DNP) function is used in the calculation. The convergence tolerance quality of geometric optimization is set to fine, the energy is set to 1×10^{-5} Ha, the maximum force is set to 0.002 Ha $Å^{-1}$, and the maximum displacement is set to 0.005 Å. The TNT model and Cu model are allowed to interact with Li. The binding energy is calculated by the following equation:

$$E_{b,TNT-Li} = E_{total,TNT-Li} - E_{TNT} - E_{Li}$$

$$E_{b,Cu-Li} = E_{total,Cu-Li} - E_{Cu} - E_{Li}$$

where $E_{b,TNT-Li}$ and $E_{b,Cu-Li}$ are the binding energies of Li^+ with TNT and Cu, respectively, $E_{total,TNT-Li}$ and $E_{total,Cu-Li}$ represent the overall energy of the TNT or Cu model combined with Li^+, E_{TNT} and E_{Cu} represent the energies of TNT and the Cu model, respectively, and E_{Li} represents the energy of Li^+.

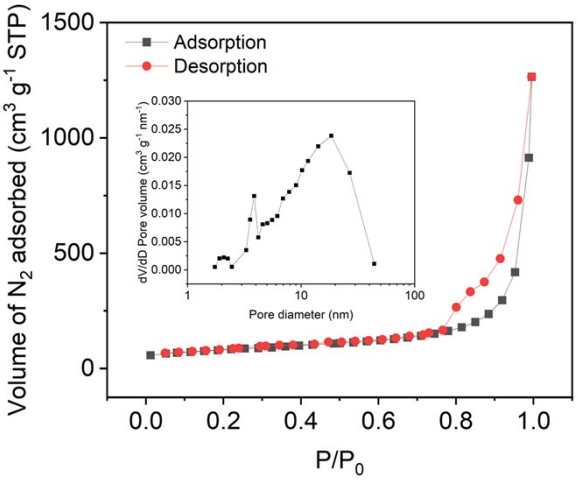

Figure S1. Isotherm of N_2 adsorption/desorption on TNT. Inset: pore size distribution (BJH desorption) of TNT.

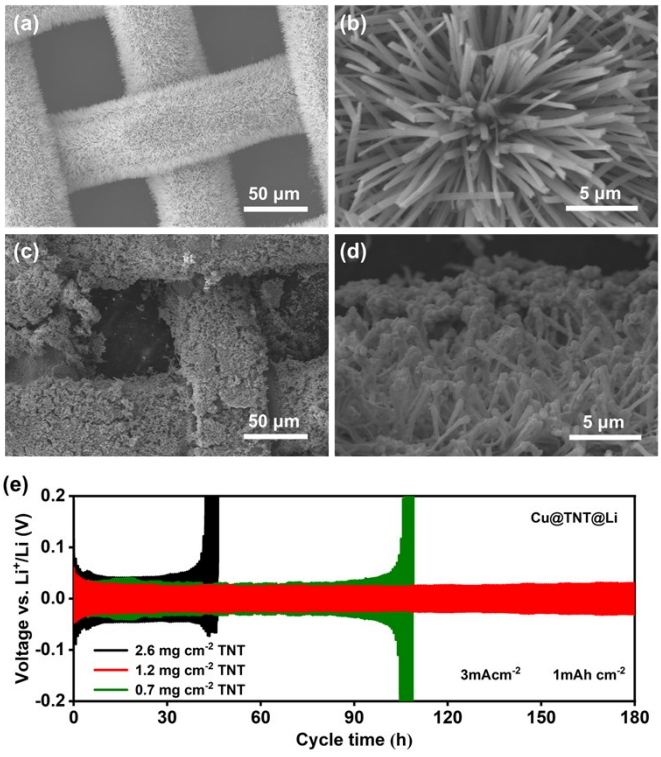

Figure S2. (a-d) SEM images of Cu@TNT electrodes with different TNT loadings: (a, b) 0.7 mg cm^{-2}, (c, d) 2.6 mg cm^{-2}; (e) galvanostatic plating/stripping cycling performance of Cu@TNT@Li symmetric cells with different TNT loadings under current density of 3 mA cm^{-2} in ether-based electrolyte.

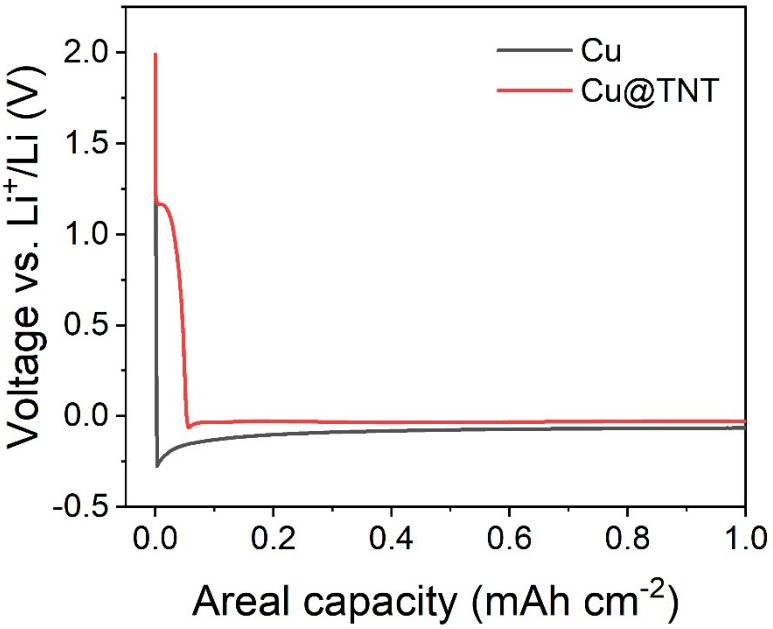

Figure S3. Comparison of the initial Li deposition curves of Cu@TNT and bare Cu mesh under 1 mA cm^{-2}.

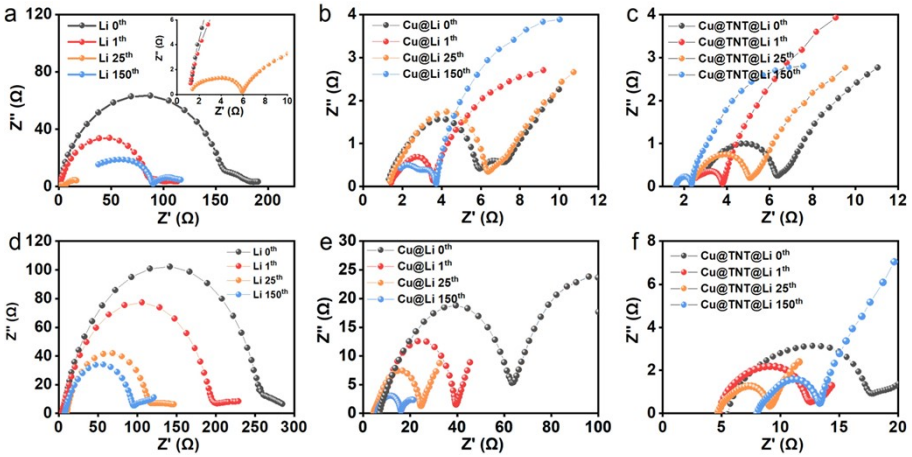

Figure S4. The Nyquist plots of different symmetric cells at different cycles in (a-c) ether-based electrolyte and (d-f) carbonate-based electrolyte.

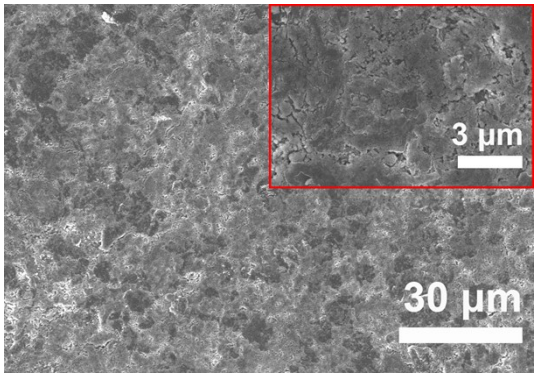

Figure S5. SEM image of Cu@TNT@Li electrode after 200 cycles in symmetric cell

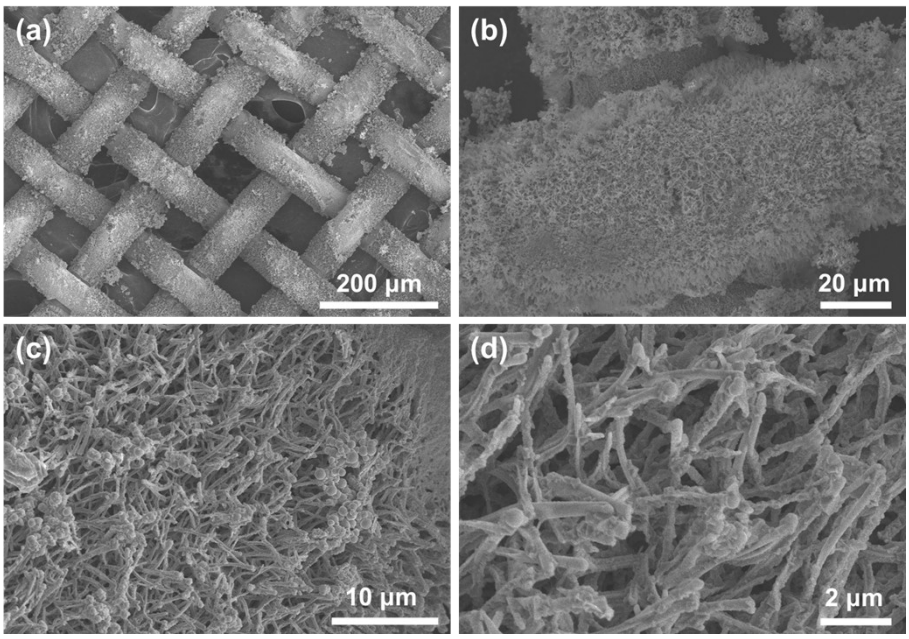

Figure S6. SEM of Cu@TNT after 200 h of plating/stripping cycling at the stripped state.

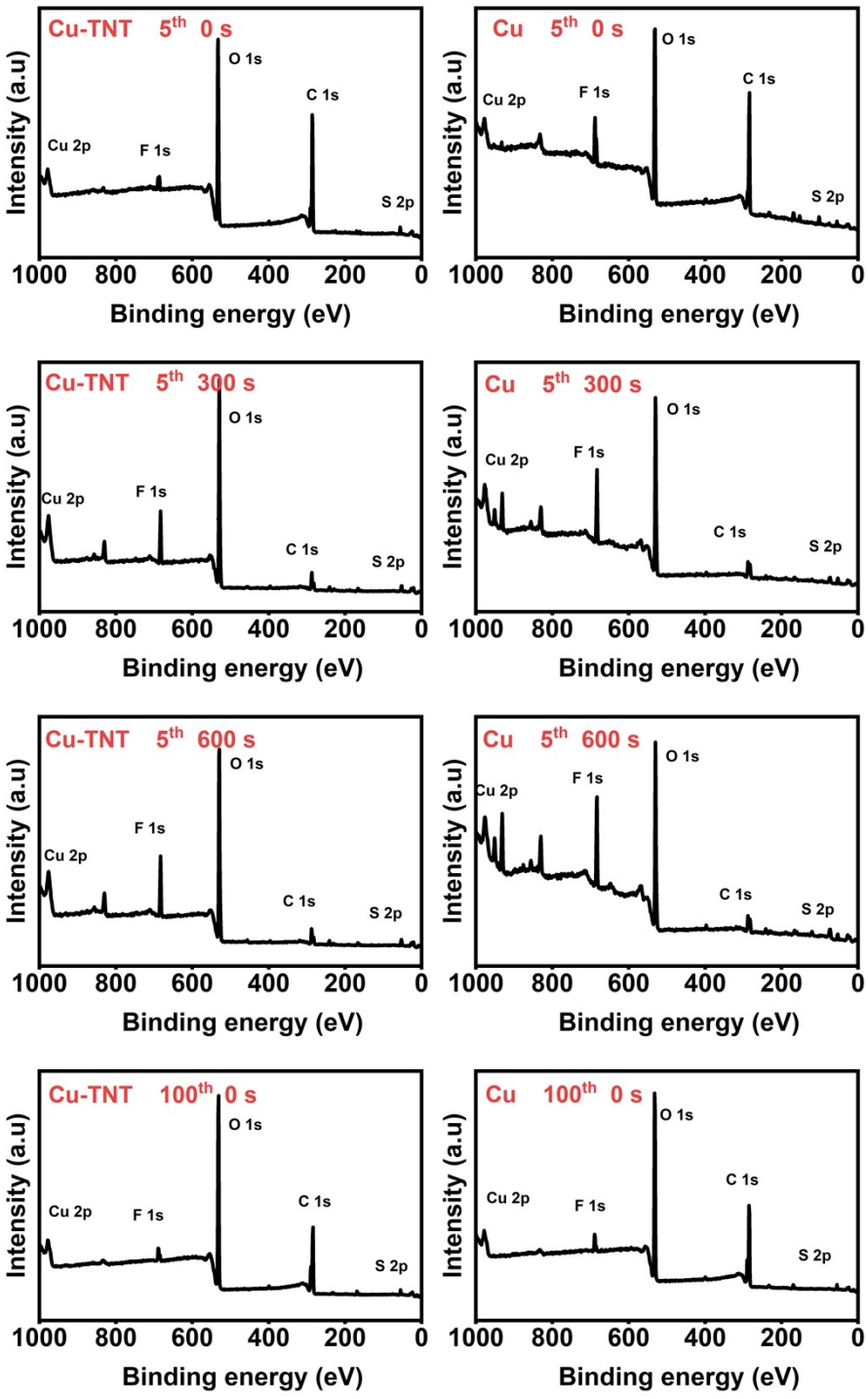

Figure S7. Survey spectra at different etching times or different cycle numbers.

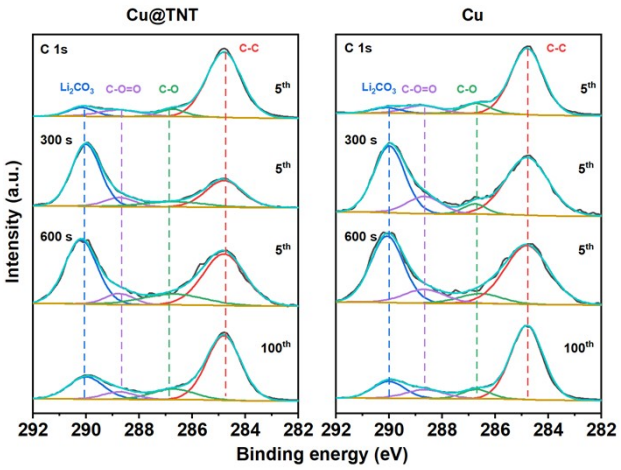

Figure S8. The C 1s spectra of surface SEI on Cu@TNT and bare Cu electrodes taken after 5 cycles and Ar etching for 0 s, 300 s and 600 s, as well as the spectra taken after 100 cycles without Ar etching.

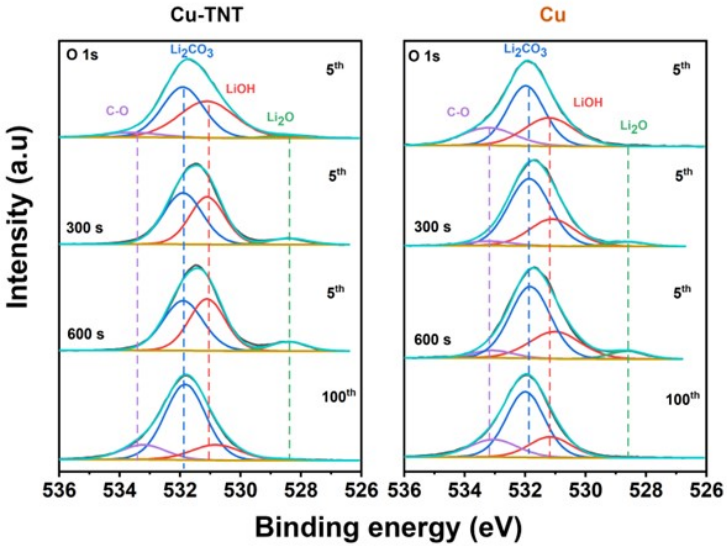

Figure S9. The O 1s spectra of surface SEI on Cu@TNT and bare Cu electrodes taken after 5 cycles and Ar etching for 0 s, 300 s and 600 s, as well as the spectra taken after 100 cycles without Ar etching.

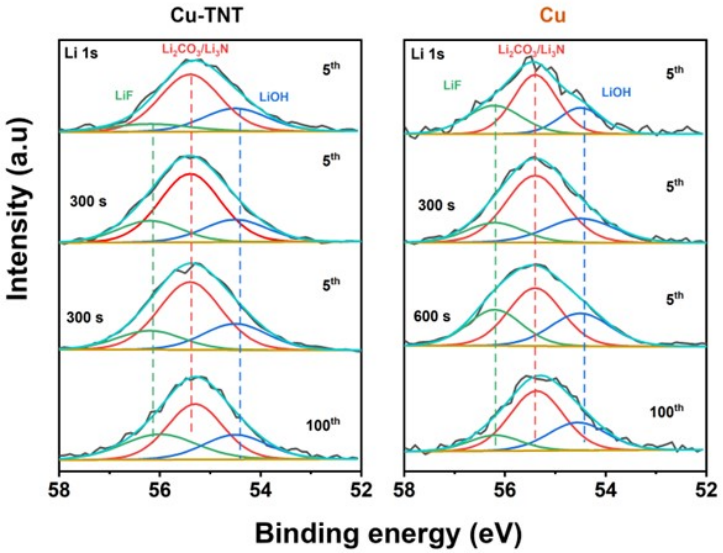

Figure S10. The Li 1s spectra of surface SEI on Cu@TNT and bare Cu electrodes taken after 5 cycles and Ar etching for 0 s, 300 s and 600 s, as well as the spectra taken after 100 cycles without Ar etching.

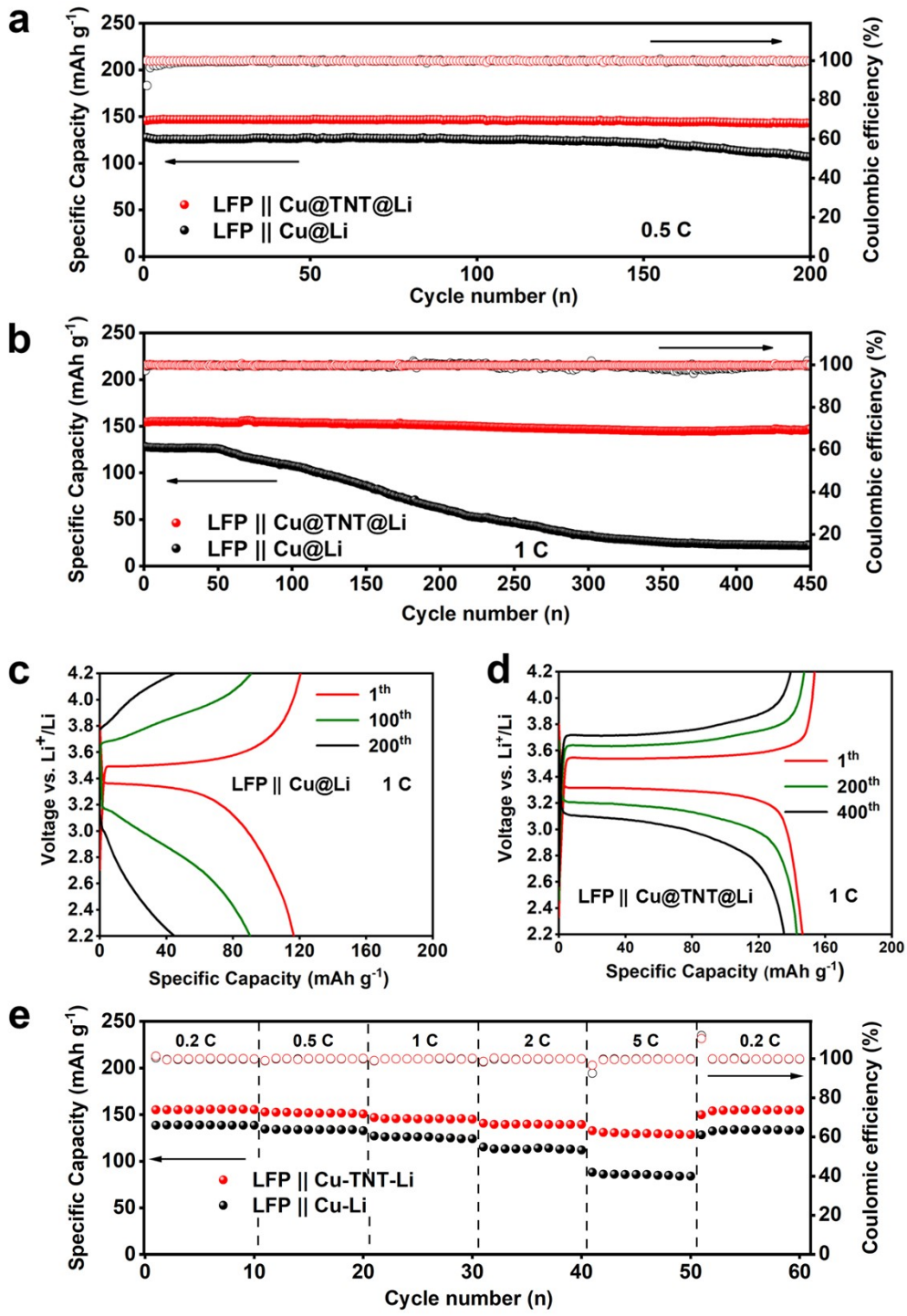

Figure S11. The full cell test results using carbonate-based electrolyte: (a, b) cycling stability of different full cells at (a) 0.5 C and (b) 1 C, (c, d) GCD curves of different full cells at 1 C, (e) rate capability of different full cells.

Table S1 Comparison of full cell cycling stability to other related reported works.

Anode	Areal capacity of Li	Areal capacity of cathode	Electrolyte	Cycling stability of full cell
Cu@TNT@Li (This work)	4 mAh cm^{-2}	1.5 mAh cm^{-2} (LFP)	1 M TFSI in DOL/DME (1:1 vol) with 1% $LiNO_3$	91.87% after 350 cycles at 1 C
CL-matrix@Li@Li_2O [1]	3 mAh cm^{-2}	0.85 and 2.1 mAh cm^{-2} (LFP)	1 M TFSI in DOL/DME (1:1 vol) with 1% $LiNO_3$	90.0% after 150 cycles at 0.5 C
TiO_2/ZnO/Li [2]	~30.7 mAh cm^{-2}	~3.58 mAh cm^{-2} (LFP)	1 M TFSI in DOL/DME (1:1 vol)	95% retention after300 cycles at 0.5 C
Li/DDTC/Cu[3]	2 mAh cm^{-2}	0.8 mAh cm^{-2} (LFP)	1 M TFSI in DOL/DME (1:1 vol) with 2% $LiNO_3$	83% retention after 300 cycles at 1 C
Ag@CMFs-Li [4]	6 mAh cm^{-2}	0.68 mAh cm^{-2} (LFP)	1 M TFSI in DOL/DME (1:1 vol) with 2% $LiNO_3$	96% retention after 250 cycles at 1 C
H-CM@Li [5]	6 mAh cm^{-2}	~2.04 mAh cm^{-2} (LFP)	1 M TFSI in DOL/DME (1:1 vol) with 1% $LiNO_3$	92% retention after 275 cycles at 1 C
M-CuO@Cu-Li [6]	3 mAh cm^{-2}	0.51 mAh cm^{-2} (LFP)	1 M TFSI in DOL/DME (1:1 vol) with 1% $LiNO_3$	88% retention after 300 cycles at 1 C

Table S2 Comparison of full cell performances to other energy storage systems.

System	Classification	Full-cell average plateau	Cycling stability of full cell
LFP‖Cu@TNT@Li (This work)	Lithium-metal battery	3.4 V	91.87% after 350 cycles at 1 C
LFP‖SSBCN [7]	Lithium-metal battery	3.2 V	92.7% after 600 cycles at 1 C
$KVPO_4F$‖PTCDI [8]	Potassium-ion battery	1.95 V	75% after 10000 cycles at 500 mA g^{-1}
KMnHCF‖PTCDI [9]	Potassium-ion battery	1.35 V	82.5% after 6500 cycles at 1500 mA g^{-1}
T-PB‖T-FeP [10]	Sodium-ion battery	2.25 V	96.8% retention after 450 cycles at 1 A g^{-1}
NVP‖CMT@Bi-C [11]	Sodium-ion battery	3.1 V	90.3% retention after 700 cycles at 1 A g^{-1}

References

[1] Z. Gong, C. Lian, P.F. Wang, K. Huang, K. Zhu, K. Ye, J. Yan, G.L. Wang, D.X. Cao, Lithiophilic Cu-Li_2O matrix on a Cu collector to stabilize lithium deposition for lithium metal batteries, Energy & Environmental Materials, 2022, 5(4), 1270-1277.

[2] Z.G. Cao, Y.B. Yang, J.L. Qin, J.Y. He, Z.X. Su, 3D TiO_2/ZnO hybrid framework: stable host for lithium metal anodes, Chemical Engineering Journal, 2022, 427, 132026.

[3] Y.J. Wang, Y. Meng, Y. Guo, D. Xiao, Achieving a dendrite-free lithium metal anode through lithiophilic surface modification with sodium diethyldithiocarbamate, Inorgnic Chemistry Frontiers, 2022, 9, 6498-6509.

[4] Y.J. Fang, S.L. Zhang, Z.P. Wu, D.Y. Luan, X.W. Lou, A highly stable lithium metal anode enabled by Ag nanoparticle-embedded nitrogen-doped carbon macroporous fibers, Science Advances, 2021, 7, eabg3626.

[5] L.Y. Ruan, X.Y. Qin, K. Lin, Z.J. Yang, Q.C. Cai, T. Li, F.T. Wu, F.Y. Kang, B.H. Li,

TiO_2/Cu_2O heterostructure enabling selective and uniform lithium deposition towards stable lithium metal anodes, Nano Research, 2023, 16, 4917-4925.

[6] Y.H. Liu, Y.F. Li, Z.Z. Du, C. He, J.X. Bi, S.Y. Li, W.Q. Guan, H.F. Du, W. Ai, Integrated gradient Cu current collector enables bottom-up Li growth for Li metal anodes: role of interfacial structure, Advanced Science, 2023, 10, 2301288.

[7] B.X. Shen, N. Fu, Y.W. Chen, W. Shao, Y.R. Yan, J. Huang and Z.L. Yang, Micron SiOx encapsulated into amorphous B, N Co-doped carbon nanotube network for high-capacity and long-durable Li-ion half/full batteries, Chemical Engineering Journal, 2023, 455, 140820.

[8] M.T. Xia, H.W. Fu, K.R. Lin, A.M. Rao, L.M. Cha, H. Liu, J. Zhou, C.X. Wang and B.A. Lu, Hydrogen-bond regulation in organic/aqueous hybrid electrolyte for safe and high-voltage K-ion batteries, Energy & Environmental Science, 2024, 17, 1255.

[9] J.M. Ge, L. Fan, A.M. Rao, J. Zhou and B.A. Lu, Surface-substituted Prussian blue analogue cathode for sustainable potassium-ion batteries, Nature Sustainability, 2022, 5, 225-234.

[10] M.W. Jiang, L.B. Ren, Z.D. Hou, W. Hua, D. Lei, Y.J. Cao, Y. Zhang and J.G. Wang, A superior sodium-ion battery based on tubular Prussian blue cathode and its derived phosphide anode, Journal of Power Sources, 2023, 554, 232334.

[11] B.H. Park, S.Y. Lee, D.Y. Han, H.K. Jiang, D.G. Seong, J.K. Yoo, S.J. Park, Y.S. Oh and J.G. Ryu, Multiscale hierarchical design of bismuth-carbon anodes for ultrafast-charging sodium-ion full battery, Applied Surface Science, 2023, 614, 156188.